HARD X-RAY FLARE SOURCE SIZES MEASURED WITH THE *RAMATY HIGH ENERGY SOLAR SPECTROSCOPIC IMAGER*

Brian R. Dennis[1] and Rick L. Pernak[1,2]
[1] Solar Physics Laboratory (Code 671), Heliophysics Science Division, NASA Goddard Space Flight Center, Greenbelt, MD 20771, USA
[2] The Catholic University of America, Washington, DC, USA

ABSTRACT

Ramaty High Energy Solar Spectroscopic Imager (*RHESSI)* observations of 18 double hard X-ray sources seen at energies above 25 keV are analyzed to determine the spatial extent of the most compact structures evident in each case. The following four image reconstruction algorithms were used: *Clean*, *Pixon*, and two routines using visibilities—maximum entropy and forward fit (*VFF*). All have been adapted for this study to optimize their ability to provide reliable estimates of the sizes of the more compact sources. The source fluxes, sizes, and morphologies obtained with each method are cross-correlated and the similarities and disagreements are discussed. The full width at half-maximum (FWHM) of the major axes of the sources with assumed elliptical Gaussian shapes are generally well correlated between the four image reconstruction routines and vary between the *RHESSI* resolution limit of $\sim 2''$ up to $\sim 20''$ with most below $10''$. The FWHM of the minor axes are generally at or just above the *RHESSI* limit and hence should be considered as unresolved in most cases. The orientation angles of the elliptical sources are also well correlated. These results suggest that the elongated sources are generally aligned along a flare ribbon with the minor axis perpendicular to the ribbon. This is verified for the one flare in our list with coincident *Transition Region and Coronal Explorer* (*TRACE*) images. There is evidence for significant extra flux in many of the flares in addition to the two identified compact sources, thus rendering the *VFF* assumption of just two Gaussians inadequate. A more realistic approximation in many cases would be of two line sources with unresolved widths. Recommendations are given for optimizing the *RHESSI* imaging reconstruction process to ensure that the finest possible details of the source morphology become evident and that reliable estimates can be made of the source dimensions.

Key words: Sun: flares – Sun: X-rays, gamma rays – techniques: image processing

1. INTRODUCTION

In the standard model of an impulsive solar flare (see, for example, Shibata et al. 1995; Shibata 1998; Tsuneta 1997), energy is released from the coronal magnetic field by a reconnection process that is still little understood. As a result, plasma is heated to tens of MK and particles—electrons and ions—are accelerated to relativistic energies. The accelerated particles spiral along the field lines on which they find themselves. Some are on open field lines and a fraction of them escape from the Sun. But generally, most are in closed magnetic loops, and they precipitate down to the footpoints, where they heat the ambient plasma primarily through Coulomb interactions. The accelerated electrons emit bremsstrahlung X-rays through interactions with the ambient ions. The accelerated ions emit gamma-rays through nuclear processes also involving the ambient ions. As a result of all the energy deposited at the loop footpoints by the accelerated particles, the ambient plasma is rapidly heated to $\gtrsim 10$ MK and the pressure differential drives it up along the field lines into the lower density corona in a process that has become known as chromospheric evaporation (see, for example, Allred et al. 2005). This hot plasma combines with the directly heated plasma already in the loop to produce the observed thermal soft X-ray (SXR) source seen in all flares. The relative contributions of directly heated and evaporated plasma to the observed SXR emission is still uncertain but it is clear that both are produced when nonthermal footpoint hard X-ray (HXR) emission is observed.

For the nonthermal footpoint HXR sources, accurate area estimates are critical in determining the energy flux in nonthermal electrons (erg s^{-1} cm^{-2}). The nonthermal electron spectrum (electrons s^{-1} keV^{-1}) is computed from the HXR spectrum (photons cm^{-2} s^{-1} keV^{-1}) assuming thick-target interactions (Brown 1971). Then, the energy flux in nonthermal electrons is calculated by integrating the thick-target electron energy spectrum (erg s^{-1} keV^{-1}) above a low energy cutoff and dividing by the source area determined from the reconstructed images.

Several recent papers have reported on measurements of HXR source sizes and the resulting electron fluxes using the *Ramaty High Energy Solar Spectroscopic Image* (*RHESSI*) imaging spectroscopy capabilities. The observations presented by Milligan et al. (2006a, 2006b) support the modeling results of Fisher et al. (1985) that show a threshold nonthermal electron flux of $\sim 3 \times 10^{10}$ erg cm^{-2} s^{-1} for the occurrence of explosive chromospheric evaporation; at lower fluxes more gentle evaporation occurs. Alexander & Daou (2007) used *RHESSI* imaging spectroscopy data for 10 flares to show that the nonthermal photon emission per unit area saturates for large flares as expected based on electron beam theories that include a return current. Xu et al. (2008) have determined sizes of extended flare structures as a function of photon energy from *RHESSI* data for 10 M-class limb events in an attempt to determine the properties (the density and length) of the electron acceleration region. Kontar et al. (2008) showed how *RHESSI* source size measurements as a function of energy for a limb flare can be used to infer the subarcsecond vertical variation of the magnetic flux tube size and neutral gas density. In all of these cases, accurate estimates of the nonthermal HXR source sizes are critical for reliable quantitative comparisons with model predictions.

HXR source dimensions at energies above $\sim$10 keV have been determined with increasing accuracy and resolution since the pioneering observations made with the HXR Imaging Spectrometer (HXIS) on the Solar Maximum Mission (SMM) in 1980 (Hoyng et al. 1981). This first evidence for double

footpoint emission at energies from 16 to 30 keV was obtained with ∼10″ resolution. Contemporaneous observations were made with the Solar X-ray Telescope (SXT) on the Japanese Hinotori mission (e.g., Tsuneta et al. 1984). More sensitive imaging observations up to ∼100 keV were made ∼10 years later by the HXR Telescope (HXT) on Yohkoh but with similar angular resolution (Kosugi et al. 1991). The *RHESSI* (Lin et al. 2002) launched in 2002 has significantly improved sensitivity with angular resolution capability of as fine as 2″3 (full width at half-maximum, FWHM) at energies from ∼3 keV to >100 keV.

All of these instruments except for HXIS use a Fourier-transform imaging technique with multiple bi-grid collimators to achieve the high angular resolution. As a result of rotating at ∼15 rpm about an axis oriented within ∼10′ of Sun-center, *RHESSI* provides measures of many more spatial Fourier components of the source region than did HXT—up to a several hundred for *RHESSI* versus 32 for HXT.

Despite *RHESSI*'s finer angular resolution, few HXR sources have been reported with spatial extents as small as 2″. This is surprising since these sources are thought to be primarily from the footpoints of magnetic loops that are known from observations at other wavelengths to be very small. Flare ribbons seen in the UV with *TRACE*, for example, are seen to be an arcsecond or so in width (e.g., Wang et al. 2007). White-light flares also show structure at the ∼1″ level (e.g., Fletcher et al. 2007; Jess et al. 2008; Wang 2009). Thus, one might expect to see HXR sources with the same width but extended along the flare ribbons. One example of such thin but extended HXR sources has been reported by Liu et al. (2007), where the HXR emission extends along the flare ribbons seen at 171 Å with *TRACE*. Even in this case, however, the FWHM resolution was only ∼ 5″9 given the *Clean* algorithm that was used. Hannah et al. (2008) reported *RHESSI* results for microflare dimensions in which they obtained mean loop lengths of 31″6 and widths of 10″5 at energies between 4 and 8 keV with very few flares with dimensions at the instrumental resolution limit of 2″3. Granted they were probably seeing the whole loop illuminated in SXRs rather than HXR footpoints, one would have expected the widths of the sources to be smaller given the extremely narrow loops seen in the EUV with *TRACE*.

In the analysis of events presented in this paper, we have tried to determine if the unexpectedly large HXR flare source sizes determined from *RHESSI* observations are accurate and reliable. We have investigated if, at least in some cases, they are the result of limited counting statistics, limitations of the Fourier-transform imaging technique used by *RHESSI*, and/or limitations of the image reconstruction algorithms currently available. In the process of this study, we have made some refinements to the standard analysis techniques to improve their capability for obtaining reliable estimates of compact HXR source sizes. The emphasis has been on making full use of data from all the *RHESSI* detectors, including those behind the finest grids when warranted by the source structure. The more extended HXR sources sometimes seen in the corona (Krucker et al. 2008) offer different challenges and are not addressed here.

In Section 2, we provide details of the *RHESSI* hardware and the currently available imaging software. We discuss modifications we have made to the software and our methodology for finding source parameters using the available image reconstruction techniques. Section 3 is a discussion of the results, the calculated source parameters, and how the modified techniques compare with each other. Our conclusions are presented in Section 4.

2. *RHESSI* IMAGING METHOD

The *RHESSI* imaging concept has been described in detail by Hurford et al. (2002). Nine nonimaging germanium X-ray/gamma-ray detectors record the deposited energy and arrival time of each photon that reaches them. A pair of grids separated by 1.5 m placed in front of each detector acts as a collimator to modulate the transmission of the incident solar X-ray flux. The grids are planar arrays of equally spaced X-ray-opaque slats separated by transparent slits. (All the grids are made of tungsten except the finest which is molybdenum.) The slits of the two grids of each subcollimator are all parallel to one another to high accuracy and their pitches are identical to a very high tolerance. As the spacecraft rotates at ∼15 rpm about an axis parallel to the subcollimator axis (to within a few arcminutes) and oriented to within a few arcminutes of Sun-center, the subcollimators modulate the transmission of incident X-rays through to the detectors. The resulting modulation of the counting rate in each detector contains encoded information about the source structure as a function of energy. The counting rate variations from a single detector in a given energy range for one modulation period can be thought of as providing the amplitude and phase of a single spatial Fourier component of all the X-ray sources on the Sun at that time. Several hundred Fourier components can be measured during one complete rotation of the spacecraft lasting ∼4 s. It is the task of the imaging software to determine the intensity and structure of the X-ray sources on the Sun that produced the modulated count rates in each detector in each energy range. The necessary aspect information is provided by the Solar Aspect System (SAS) and the PhotoMultiplier-Tube Roll Angle System (PMTRAS), which provide the absolute orientation of the spacecraft with subarcsecond accuracy several times per second.

2.1. Image Reconstruction Techniques

We have used, with some modifications, all of the image reconstruction algorithms currently available in the online SolarSoftWare (SSW) collection of IDL procedures to generate *RHESSI* images. The basic techniques described by Hurford et al. (2002) include back projection, *Clean*, the *Pixon* method, the maximum entropy method (MEM), and forward fitting. More recently, refinements of two of these techniques based on the use of visibilities have become available—*MEM_NJIT* (Schmahl et al. 2007) and visibility forward fit (*VFF*; Hannah et al. 2008). A brief description of each method is first given below. We then describe the procedures we have used to optimize the methods used for determining the dimensions of the most compact sources and to allow quantitative comparisons to be made between the different results.

Back projection basically projects each detected photon back from the detector through the slits of the grid pairs to all possible locations for its origin on the Sun. This creates a probability map made up of parallel ridges aligned with the slit orientation at that time. The spacing between ridges is equal to twice the FWHM resolution of the subcollimator. This back projection is repeated for each detected photon and the resulting probability maps are summed to form the so-called dirty map. (In practice, to save computer time, the same probability map is used for all counts that occur in time bins short compared to the modulation time at each roll angle.) The dirty map shows the real source or sources convolved with the point-spread function (PSF) for the specific combination of grids that were used. The PSF is essentially the dirty map that would result from a single point

source on the Sun. It consists of an approximately Gaussian central peak with multiple concentric circular side lobes. The FWHM of the Gaussian depends on the detectors and the type of weighting that are used. The current options available in the *RHESSI* software are "uniform weighting" that emphasizes the finer grids by using weights that are inversely proportional to the collimator angular resolution, and "natural weighting" that weights all detectors equally.

The task for *Clean* is to determine what set of *point* sources could have produced the dirty map obtained from the back projection routine given the instrument PSF. The *Clean* algorithm first finds the pixel with the highest flux in the dirty map. It assigns a point source at the same location in a new map of *Clean* components with a fixed fraction (known as the "loop gain") of that flux. It then subtracts that same fractional flux from the dirty map but spread out according to the PSF centered on the same pixel. This process is repeated by taking the pixel with highest flux in the new dirty map, the so-called residual map. Cycling through this process can be continued a specified number of times or until the peak absolute flux in the residual map is negative. The information from this process is the list of *Clean* point-source components with their fluxes and locations. In order to display these point sources in an image, the default version of *Clean* convolves them with the so-called *Clean* beam, a Gaussian whose width is approximately equal to the width of the central peak of the PSF. (Actually, the default *Clean* beam used in the software has the same curvature at the peak as the PSF.) This Gaussian must be removed in quadrature when estimating source sizes; failure to do so has led to significant overestimation in some cases. Unless this is done, the source sizes obtained with the default version of *Clean* are significantly larger than those obtained with the other algorithms (Schmahl et al. 2007). Another aspect of the default version of *Clean* is that the displayed image has the remaining residual map added to the component point sources after convolution to provide a visual indication of the noise. This too handicaps *Clean* in comparison with the other techniques, where this is not done by default.

An indication of the different ways of using *Clean* is indicated in the top half of Figure 1, where different grid combinations were used in obtaining the images. The large difference in source sizes is apparent between the standard version using grids 3–9 (top left image) and grids 1–9 (center top image). For our analysis in this paper, we have used only the *Clean* point-source components obtained with all nine detectors (top right image). As the result of convolving the point-source components with the "*Clean* beam," the default version made using grids 3–9 shows the sources in this case to be about a factor of ~3 larger in extent than indicated by the components alone. The images obtained with the other three algorithms are shown for comparison in the bottom half of the figure.

The *Pixon* algorithm used for the reconstruction of images from *RHESSI* data is an adaptation of the program successfully used to analyze data from Yohkoh/HXT (Metcalf et al. 1996). Unlike *Clean*, which models the source as a collection of point sources, this algorithm seeks a superposition of circular sources or pixons of different sizes and parabolic profiles that best reproduces the measured modulations from the different detectors. The goal is to construct the image with the fewest degrees of freedom (the fewest pixons) that is consistent with the observations (i.e., the image predicts the modulated count rates with a value of χ^2 per degree of freedom acceptably close to one). This technique is generally thought to provide the most

accurate image photometry (Alexander et al. 1997) but at the price of taking well over an hour per 128×128 pixel image even on the fastest available PC. As with the other reconstruction algorithms, the *Pixon* technique as currently implemented can have difficulties with the most compact sources breaking up when the finest grids are used. This problem can be alleviated with various user-controlled parameters but it raises questions about the validity of the dimensions obtained in these cases.

The MEM approach differs from *Pixon* and *Clean* in that it assumes that each pixel of the image is an independent source, i.e. there are 128×128 degrees of freedom for the image size typically used. The algorithm iteratively searches for that image where the flux in each pixel is constrained by the requirements that the entropy is maximized while the value of χ^2 is acceptable, i.e., the image is the flattest possible consistent with the observations. *MEM_NJIT* (Schmahl et al. 2007) implements this approach through the use of "visibilities" instead of the count-rate modulation profiles used by *Clean* and *Pixon*. A visibility is a measure of a single spatial Fourier component of the image. It is derived from the sinusoidal component of the variation of the *RHESSI* source count rate from a single detector as the spacecraft rotates through a small roll angle. All effects of pointing excursions, grid transmission variations, detector sensitivities, etc., are taken into account so that each visibility is a property of the source distribution alone. It can be characterized by an amplitude and a phase, or equivalently, a real (cosine) and an imaginary (sine) component. *MEM_NJIT* as currently implemented is very fast, and Schmahl et al. (2007) found that it gives maps that are morphologically and photometrically similar to those obtained with *Pixon*. It too is subject to source breakup when using data from the finest grids. However, real "super-resolution" by up to a factor of 2 or 3 times better than the width of the system's PSF is known to be possible under certain circumstances (Cornwell & Evans 1985; Narayan & Nityananda 1986).

The original forward-fit algorithm (Aschwanden et al. 2002) starts with the assumption that there are a very limited number of individual sources, usually only one or two. The parameters describing each source (e.g., the flux, location, size, and orientation of an elliptical Gaussian) are adjusted until the model-predicted count rates agree best with the measured count rates in a χ^2 sense. The new visibility version of forward fit, *VFF*, adjusts the source parameters such that the model-predicted visibilities agree best with the measured visibilities (Hannah et al. 2008). This approach offers fast determinations of these source parameters. However, as with any forward-fitting method, it is critical that the assumptions concerning the number of sources and their shapes match reality. In the current default version of *VFF*, one can only image a single circular or elliptical Gaussian, or single loop, or two circular Gaussians. We have modified *VFF* to handle two elliptical Gaussians (see below).

2.2. Data Analysis

Since we are primarily interested in determining the spatial extent of the most compact HXR sources, we have used the flares analyzed by Schmahl et al. (2007) as a guide for our sample. The 25 flares used for that paper were chosen from the images made and put on line at the HESSI Experimental Data Center (HEDC) at ETH Zurich (http://hercules.ethz.ch:8081/www/index.html; Saint-Hilaire et al. 2002). The ~1 minute time interval during each flare used in the analysis was chosen to have well-resolved double HXR sources (believed to be footpoints) with sufficient intensity to provide $>10^4$ counts summed over all
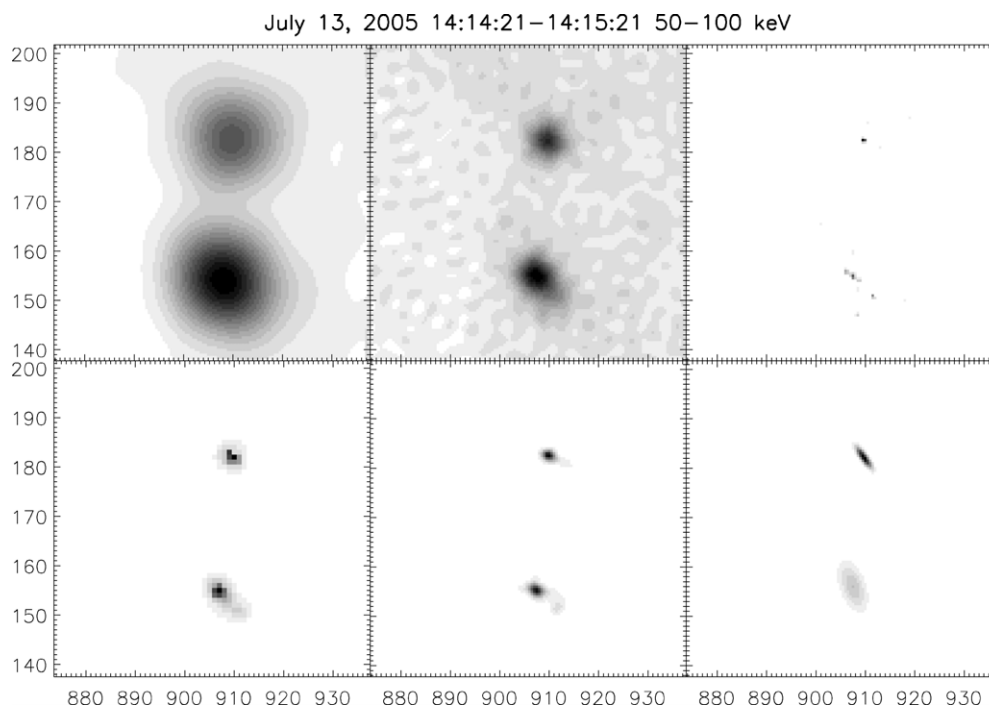
Figure 1. Images of M5.1 flare (flare 15 in Table 1) on 2005 July 13 from 14:14:21 to 14:15:21 UT in the 50–100 keV energy range made with all four of the reconstruction algorithms. Top three images all made with *Clean*. The left image was made using the default settings including detectors 3–9, natural weighting, convolved with the "*Clean* beam" and residuals included. Center image is made with detectors 1–9. Right image made the same way but showing the components only. Bottom three images are for the same time interval and energy range and using detectors 1–9. They were made using *Pixon* (left), *MEM_NJIT* (center), and *VFF* (right).

nine detectors at energies above 25 keV. If there were multiple images satisfying these criteria for a given flare, then the interval with the most counts was selected. Schmahl et al. (2007) did not use the coarsest or the finest grids in their analysis since they were primarily interested in testing the then-new *MEM_NJIT* procedure itself and were not concerned with determining the finest source sizes. In this study, we chose only those 18 flares of the 25 that still appeared to be double sources when all nine of *RHESSI*'s detectors were used in the image reconstruction. The other seven flares showed evidence of additional sources that could not be modeled with our version of *VFF*, which is limited to considering up to two elliptical Gaussian sources. Details of the 18 flares in our sample are listed in Table 1. In retrospect, it became clear that some of these 18 flares also show evidence for more than two distinct sources but this was not apparent in the initial flare selection.

We have used modified versions of each of the four image reconstruction methods described above in order to optimize their ability to provide accurate information on the most compact sources. To be able to compare the results from the different methods, we have also used procedures to allow the parameters of the equivalent elliptical Gaussians to be determined for the sources in each case. Two sources are considered for each flare and labeled as "Source 1" for the stronger of the two and "Source 2" for the weaker, except where the fluxes are within 1σ of each other.

We have adapted the default version of *Clean* so that the source sizes are derived directly from the *Clean* point-source components themselves rather than from the standard map. Figure 1 shows the sources obtained in this way for the flare on 2005 July 13 in comparison with the sources obtained using the default version of *Clean* and the other reconstruction algorithms. Comparisons of the different techniques are also shown for two other events in Figure 2. The procedure we used

Table 1
Flare Dates, Times, and Energy Ranges Used in the Analysis

Flare No.	Date	Time Interval (UT)	GOES Class	Energy (keV)	Counts[a] ($\times 10^4$)
1	2002 Feb 20	11:06:00–11:06:36	C8.3	25–50	5.35
2	2002 Jul 23	00:41:00–00:42:00	X5.1	50–100	5.72
3	2002 Sep 08	01:42:20–01:43:20	M1.6	25–50	7.71
4	2002 Sep 20	09:26:08–09:27:08	C5.4	25–50	5.69
5	2002 Nov 09	13:21:04–13:22:04	M4.9	25–50	13.6
6	2003 Mar 18	12:14:00–12:15:00	X1.5	50–100	4.16
7	2003 Jun 09	11:24:12–11:25:12	M4.8	50–100	7.20
8	2003 Jun 10	11:06:16–11:07:16	M5.4	25–50	3.76
9	2003 Oct 24	02:55:52–02:56:52	M7.7	25–50	8.07
10	2003 Nov 19	03:59:28–04:00:28	M1.8	25–50	8.27
11	2004 Nov 06	00:30:24–00:31:24	M9.5	50–100	3.02
12	2004 Dec 01	07:09:56–07:11:56	M1.2	25–50	5.02
13	2005 Jan 15	22:42:46–22:44:20	X2.7	25–50	18.8
14	2005 Jan 20	06:45:08–06:46:08	X7.1	50–100	206
15	2005 Jul 13	14:14:21–14:15:21	M5.1	50–100	5.96
16	2005 Jul 30	06:30:30–06:33:30	X1.3	50–100	29.3
17	2005 Aug 22	17:04:16–17:05:16	M6.3	25–50	14.3
18	2005 Sep 10	21:32:00–21:34:00	X2.1	50–100	8.13

Note.
[a] Total number of *RHESSI* counts in the specified energy range used to make the images.

to determine the source sizes using *Clean* is as follows: first we ran *Clean* using all nine detectors, natural weighting, a loop gain of 5%, and stopping the process of selecting point-source components when the peak absolute flux in the residual map is negative. This usually results in over 100 iterations. Then the map of the *Clean* components is used rather than the usual map with the components convolved with the *Clean* beam. The sources are located visually from the clustering of components.
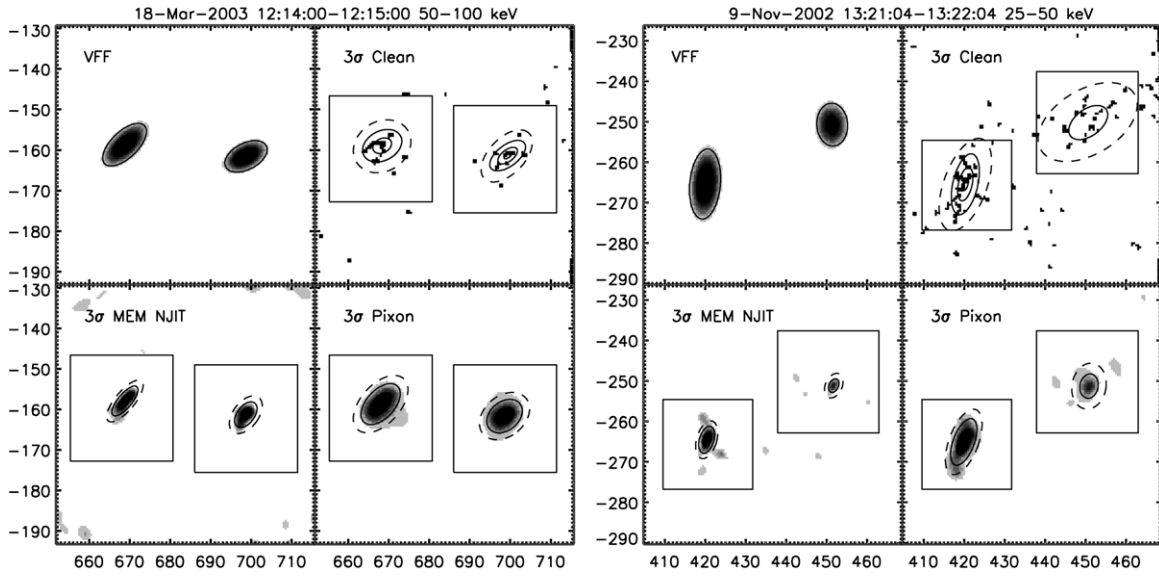
Figure 2. Images for the 2003 March 18 and 2002 November 9 flares made with the four reconstruction techniques. The source parameters are given in Tables 2 and 3, respectively. The gray scale shows the two sources in each case with contour levels at 10%, 50%, and 90% of the maximum of the associated elliptical Gaussians fitted to the data inside the user-defined rectangles. The dashed lines show the 3σ ellipses (see the text). The user does not define regions for the sources in *VFF* and consequently no rectangles or 3σ ellipses are shown. Note that for clarity the individual point source components in the *Clean* images are all shown as black $1'' \times 1''$ pixels so information about their relative intensities is not evident.

A rectangle is defined around each source that contains all of the components that are judged to belong to that source. The first and second moments of these components are then computed for the source within this rectangle as a function of the azimuthal angle about the source. The first moment locates the source centroid inside the rectangle, while the highest and lowest second moments give the sigmas of the major axis (*a*) and the minor axis (*b*) of the equivalent elliptical Gaussian, respectively. (Note that this method does not allow for any background or more extended source that might form a pedestal on which the compact source sits, whereas the method used to determine the source dimensions from the *Pixon* and *MEM_NJIT* images does—see below.) The orientation angle is the azimuthal angle at which the second moment of the *Clean* components is a maximum. A final step to reduce the subjectivity of the initial rectangles is to eliminate all outlier components $>3\sigma$ from the source centroid location and repeat the calculations. This method is then referred to as 3σ *Clean*. The source eccentricity, *e*, is related to *a* and *b* as follows:

$$e = \sqrt{1 - (b/a)^2}. \qquad (1)$$

An estimate of the source area (*A*) of the elliptical Gaussian within 1σ of the centroid is calculated from the relation,

$$A = \pi ab. \qquad (2)$$

Conversion from the 1σ values (*a* and *b*) to the FWHM of the major and minor axes is made using the relation,

$$\text{FWHM} = 2\sigma \sqrt{-2\ln \tfrac{1}{2}} \approx 2.35\sigma. \qquad (3)$$

For *Pixon* and *MEM_NJIT*, we have run the procedures with the default settings but obtained the parameters of the equivalent elliptical Gaussian for each of the sources in a manner similar to that described above for *Clean*. In this case however, we use the IDL program GAUSS2DFIT to obtain the same set of best-fit parameters for each source inside user-defined rectangles.

As with *Clean*, we eliminate all outlier components inside the ellipse located $>3\sigma$ from the source center and add "3σ" to the method name.

We have altered *VFF* so that it can fit two elliptical Gaussians to the data in any given time interval. Thus, there are a total of 12 free parameters, the following six for each source: flux, *x*-position, *y*-position, major axis FWHM, eccentricity, and orientation angle. These parameters can then be compared directly with the same parameters derived from the other routines for the same two sources. Note, however, that significant differences can arise if the sources are not well approximated by elliptical Gaussians or if the image contains more than two sources.

In comparing the results of the different image reconstruction algorithms, it is important to know the magnitude of the uncertainties. However, except for *VFF*, no provision is made for estimating uncertainties on the source parameters in the current versions of the imaging algorithms. With *VFF*, the statistical uncertainties on the visibility parameters are readily calculated, and the image reconstruction procedure is very fast. Consequently, uncertainties on the derived source parameters can be determined using the Monte Carlo technique of randomly varying the visibilities and recalculating the source parameters a large number of times. The $\pm 1\sigma$ uncertainties calculated in this way (σ_{VFF}) are given for the *VFF* fit parameters listed in both Tables 2 and 3. For our current purposes, we have assumed that the source parameter uncertainties are similar for the other reconstruction algorithms. We plan to test this assumption in the future by varying the measured modulated count rates within the expected Poisson uncertainties and recomputing the images many times. This will be very time consuming for the other methods although we hope to be able to use the computed uncertainty map that is automatically computed as part of the *Pixon* algorithm.

3. RESULTS

Figure 2 shows images for two events determined with the four algorithms—*VFF*, *Clean*, *MEM_NJIT*, and *Pixon*—

Table 2
Source Parameters for the Flare on 2003 March 18 Between 12:14:00 and 12:15:00 UT

Algorithm	Flux (photons cm^{-2} s^{-1})	Major Axis a (″)	Minor Axis b (″)	Eccentricity e	Area πab (arcsec^2)	Orientation (° E of N)
Source 1						
VFF[a]	7.7 ± 0.3 (4.7)[b]	2.6 ± 0.3 (0.7)	1.3 ± 0.4 (0.8)	0.94 ± 0.05 (1.8)	10 ± 4 (1.0)	134 ± 16 (0.1)
3σ Clean	6.6 (1.0)	2.9 (0.3)	2.1 (1.3)	0.71 (2.8)	19 (1.3)	118 (0.9)
3σ MEM_NJIT	5.1 (4.0)	2.5 (1.0)	0.9 (1.8)	0.93 (1.6)	7 (1.8)	140 (0.4)
3σ Pixon	5.8 (1.7)	3.4 (2.0)	2.0 (1.0)	0.82 (0.6)	21 (1.8)	138 (0.3)
Mean[c]	6.3	2.8	1.6	0.85	14	133
Source 2						
VFF[a]	6.7 ± 0.3 (4.7)[b]	2.3 ± 0.4 (0.5)	1.3 ± 0.5 (0.4)	0.8 ± 0.10 (0.1)	10 ± 5 (0.4)	120 ± 39 (0.3)
3σ Clean	5.4 (0.3)	2.8 (0.8)	1.4 (0.2)	0.86 (0.7)	13 (0.2)	127 (0.1)
3σ MEM_NJIT	4.4 (3.0)	2.1 (1.0)	1.2 (0.6)	0.81 (0.2)	8 (0.8)	143 (0.4)
3σ Pixon	4.6 (2.3)	2.8 (0.8)	2.0 (1.0)	0.69 (1.0)	18 (1.2)	130 (0.4)
Mean[c]	5.3	2.5	1.5	0.79	12	129

Notes. In the energy range from 50 to 100 keV—see Figure 2 (left).
[a] The ±1σ uncertainties are given for the VFF parameters only.
[b] The number in parentheses in each case is the deviation from the mean value expressed in units of the VFF 1σ uncertainty.
[c] The mean is the average of the four values found for a given parameter with the different image reconstruction methods.

Table 3
Source Parameters for the Flare on 2002 November 9 Between 13:21:04 and 13:22:04 UT

Algorithm	Flux (photons cm^{-2} s^{-1})	Major Axis a (″)	Minor Axis b (″)	Eccentricity e	Area πab (arcsec^2)	Orientation (° E of N)
Source 1						
VFF[a]	33 ± 1 (8.0)[b]	3.1 ± 0.2 (0.5)	1.3 ± 0.2 (0.5)	0.93 ± 0.02 (1.3)	13 ± 2 (1.0)	175 ± 5 (1.5)
3σ Clean	30 (5.0)	4.2 (5.0)	1.7 (1.5)	0.92 (0.8)	22 (3.5)	167 (0.2)
3σ MEM_NJIT	14 (11.0)	1.9 (6.5)	1.0 (2.0)	0.86 (2.3)	6 (4.5)	164 (0.3)
3σ Pixon	23 (2.0)	3.5 (1.5)	1.5 (0.5)	0.91 (0.3)	17 (1.0)	159 (1.2)
Mean[c]	25	3.2	1.4	0.91	15	166
Source 2						
VFF[a]	17 ± 2 (3.0)[b]	2.7 ± 0.3 (0.3)	1.9 ± 0.4 (0.0)	1.0–0.06 (3.2)	16 ± 5 (0.6)	173 ± 22 (0.9)
3σ Clean	14 (1.5)	4.5 (5.7)	2.9 (2.5)	0.80 (0.2)	41 (4.4)	125 (1.1)
3σ MEM_NJIT	3 (4.0)	1.3 (5.0)	0.8 (2.8)	0.77 (0.7)	3 (3.2)	155 (0.1)
3σ Pixon	8 (1.5)	2.6 (0.7)	2.0 (0.3)	0.67 (2.3)	17 (0.4)	170 (0.4)
Mean[c]	10.5	2.8	1.9	0.81	19	156

Notes. In the energy range from 25 to 50 keV (see Figure 2, right).
[a] The ±1σ uncertainties are given for the VFF parameters only.
[b] The number in parentheses in each case is the deviation from the mean value expressed in units of the VFF 1σ uncertainty.
[c] The mean is the average of the four values found for a given parameter with the different image reconstruction methods.

modified as indicated above. The left half has images for the 2003 March 18 flare. They show, at least qualitatively, that the two sources have similar shapes and orientations and that elliptical Gaussians are good approximations to the data in all cases. A quantitative comparison of the source parameters determined with the four modified algorithms is provided in Table 2. The best-fit values for each parameter are given for each algorithm but ±1σ uncertainties are given only for the VFF values (σ_{VFF}). The mean values obtained by averaging over all algorithms are also listed for each source. (Note that the number given in parentheses after each value is not its 1σ uncertainty but rather the number of σ_{VFF} uncertainties that the value differs from the mean value.) Except for the flux, most of the parameters are within ±1σ_{VFF} of the mean value and all are within ±2σ_{VFF} of the mean. The larger disparities in fluxes are discussed in Section 3.1.

The right half of Figure 2 is for the 2002 November 9 flare. It is apparent that there are differences in source extent and orientation angle of the two sources as they appear in the four images. Inspection of Table 3 shows that there is good agreement in orientation angle for all algorithms and both sources (all

measurements are within the estimated ±2σ_{VFF} of the mean), though the uncertainty in the measurement for the weaker Source 2 is larger. However, source dimensions can differ by >3σ_{VFF}. In particular, MEM_NJIT and Clean give values of the major axis for both sources that differ substantially from the average of all the measurements, with MEM_NJIT being lower and Clean higher than the mean by ⩾ 5σ_{VFF}. Consequently, the calculated areas also differ by similar factors in these cases.

A possible explanation for differences in elliptical parameters with the weaker source in the 2002 November 9 event is that there appears to be other sources in the image. The MEM and the Pixon images in Figure 3 both show other weak sources in addition to the two major peaks. Some of these weak sources have comparable total fluxes to our "Source 2." Those that lie within the user-defined rectangle will significantly alter the estimates of the parameters of the elliptical Gaussians representing that source. The backgrounds of the two surface plots in Figure 3 differ significantly in that Pixon's background is much flatter than that of MEM_NJIT, but the Pixon "subsources" are more prominent—larger and brighter. This is presumably why Source 2 in Pixon is at least double the flux and extent
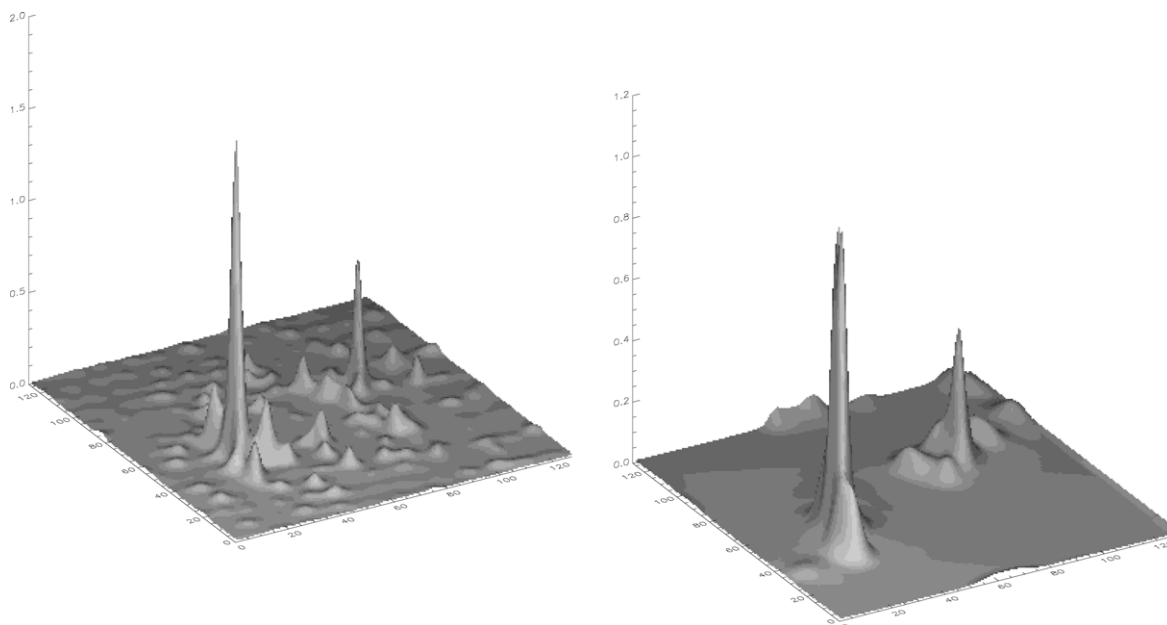
Figure 3. Surface plot obtained using *MEM_NJIT* (left) and Pixon (right) in the 25–50 keV energy range for the 2002 November 9 flare in the 1 minute interval after 13:21:04 UT.

(major and minor axes) of Source 2 in *MEM_NJIT*. The significance of these weaker sources and their effect on *VFF* measurements are discussed in Section 3.3.

3.1. Comparison of Elliptical Parameters

The elliptical Gaussian source parameters determined using all four of the image reconstruction techniques are compared in Figures 4–7 for all 18 flares studied. In each panel of each figure, a source parameter determined by one method is plotted versus the same parameter determined by a different method for all 18 flares, two sources per flare.

The source fluxes determined by the different methods are highly correlated as shown in Figure 4. The correlation coefficient in the lower right-hand corner of all six plots is $\geqslant 0.97$ in all cases. However, there are systematic differences between the fluxes determined from the different image reconstruction methods.

An explanation of the higher *VFF* fluxes is given in Section 3.3. *Clean* surprisingly yields higher fluxes than *MEM_NJIT* and *Pixon* in contradiction to the results of Schmahl et al. (2007). This is even more unexpected since we have adopted the nonstandard approach of ignoring the flux contribution of the *Clean* residuals. The cause of this discrepancy is not known at this time. One difference that may be significant is that in using GAUSS2DFIT to determine the best-fit elliptical Gaussians to the *MEM_NJIT* and *Pixon* sources, a constant term is included for any pedestal that might exist inside the user-defined rectangle around each source. No such pedestal is subtracted in the analysis of the *Clean* sources.

Major and minor axes FWHM values are compared in Figures 5 and 6. The major axes values generally show good correlation between all algorithms except *VFF* with the correlation coefficient >0.79. The correlation coefficient when *VFF* values are involved is <0.71. For the minor axis the correlations are quite poor with a coefficient of <0.51. The one exception is the correlation between the *VFF* and *MEM_NJIT* with a coefficient of 0.70. The source orientation angles, measured in degrees east of north (i.e., counterclockwise on the Sun), are in

excellent agreement between all the algorithms with correlation coefficients $\geqslant 0.8$ (see Figure 7).

It is expected that these HXR footpoint sources will be aligned along the flare ribbons seen at other wavelengths. We have checked this for the flare on 2005 July 30 with the *TRACE* images at 171 Å that show two clear ribbons—see Figure 8. The two HXR sources do indeed lie on the two ribbons after the *TRACE* image is offset to match the near coincident EIT image at 195 Å. The orientation of the north-eastern HXR source is indeterminate since it is almost circular, and indeed, it coincides with a bright part of the EUV ribbon where it changes direction by $\sim 90°$. The south-western source, however, is clearly aligned north–south along the western ribbon. Thus, it appears that the orientation angle of this weaker source is accurate to within the $10° 1\sigma$ uncertainty that we have estimated. Unfortunately, the other flares in our analysis do not have corresponding *TRACE* images, so no other comparisons could be made.

3.2. Distributions of Source Sizes

Frequency histograms of major and minor axes are displayed in Figures 9 and 10, respectively. We find that the mean length of the major axis is ~ 6–$7''$ depending on the algorithm used, and the mean minor axis is ~ 3–$4''$. The modified version of *Clean* gives less spread than the other three algorithms—$\sigma = 3''$ versus 3.5–$4''$ for the other algorithms but this is mainly the result of just a few outliers.

Our results are not consistent with Hannah et al. (2008), whose mean source width is $11''$. However, the events in their study were microflares that were generally only detected at energies below 20 keV. Consequently, they did not use the two finer grids, namely detectors 1 and 2. Detector 1 has a FWHM angular resolution of $2.''3$, smaller than any of their sources, so usage of this subcollimator with flare loops only adds noise to the map; detector 2 is not generally sensitive to energies below ~ 20 keV. There are no such limitations in our sample, since we examine compact HXR sources in the 25–100 keV range, so we are able to take advantage of the resolution of the finer grids.
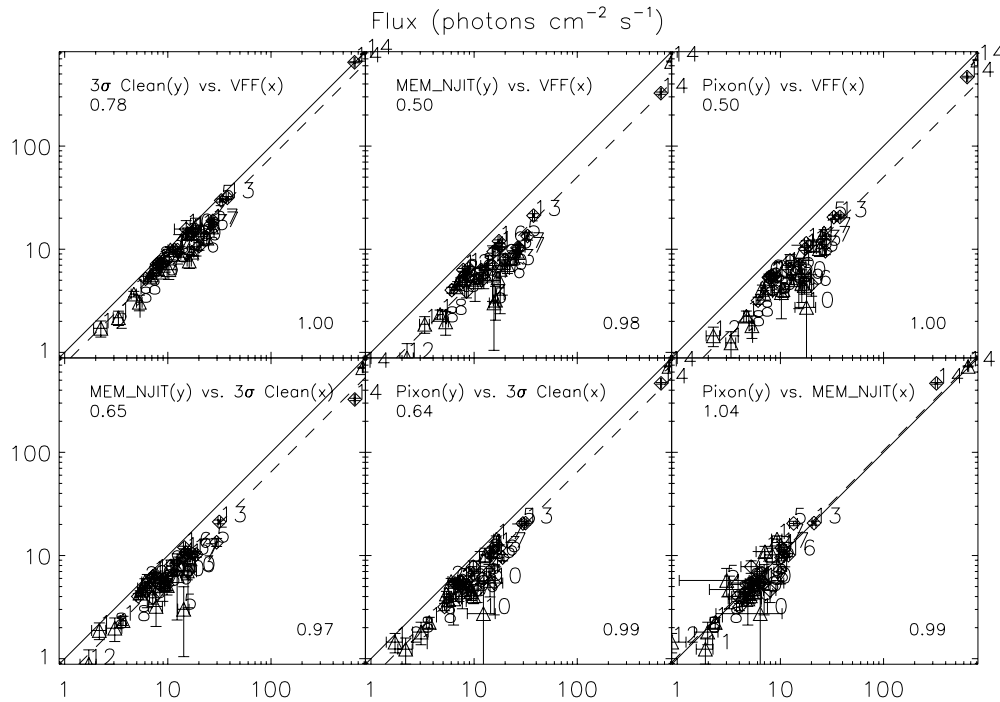
Figure 4. Plots of source flux measurements for both sources of all 18 flares in our sample. The fluxes derived from the different algorithms are plotted against one another as indicated in the top left of each plot. The numbers in the upper left denote the average ratio of flux in the y-direction to the flux in the x-direction, and the dashed line represents this systematic shift. Correlation coefficients are displayed in the bottom right-hand corner of each plot to show the agreement between the compared algorithms.
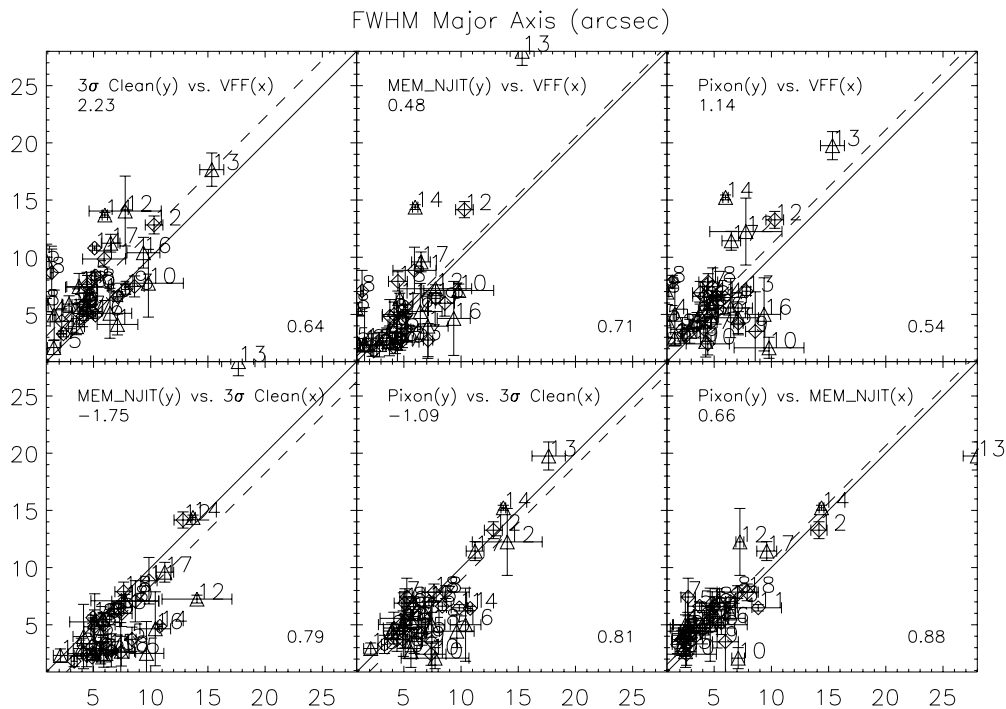
Figure 5. Major axes comparison. Axis labels follow the template used in Figure 4. The numbers in the upper left denote the average difference between major axis measurements in the y-direction and major axis measurements in the x-direction. The dashed line represents this systematic shift in the $y = x$ line.

3.3. Additional Sources

As noted in Section 3.1, the flux values obtained using *VFF* tend to be systematically higher than the values obtained from the other image reconstruction methods (see Figure 4). Possible explanations for this discrepancy could be the presence of more than two compact HXR sources or the existence of

an extended component, possibly the albedo from the lower solar atmosphere. Since *VFF* uses a model with only two sources and minimizes χ^2, it effectively adds in flux from any other sources—additional footpoints, coronal sources, or albedo flux—into the two model sources. The other three algorithms allow additional HXR sources to be included at the correct location in the image without necessarily affecting the two
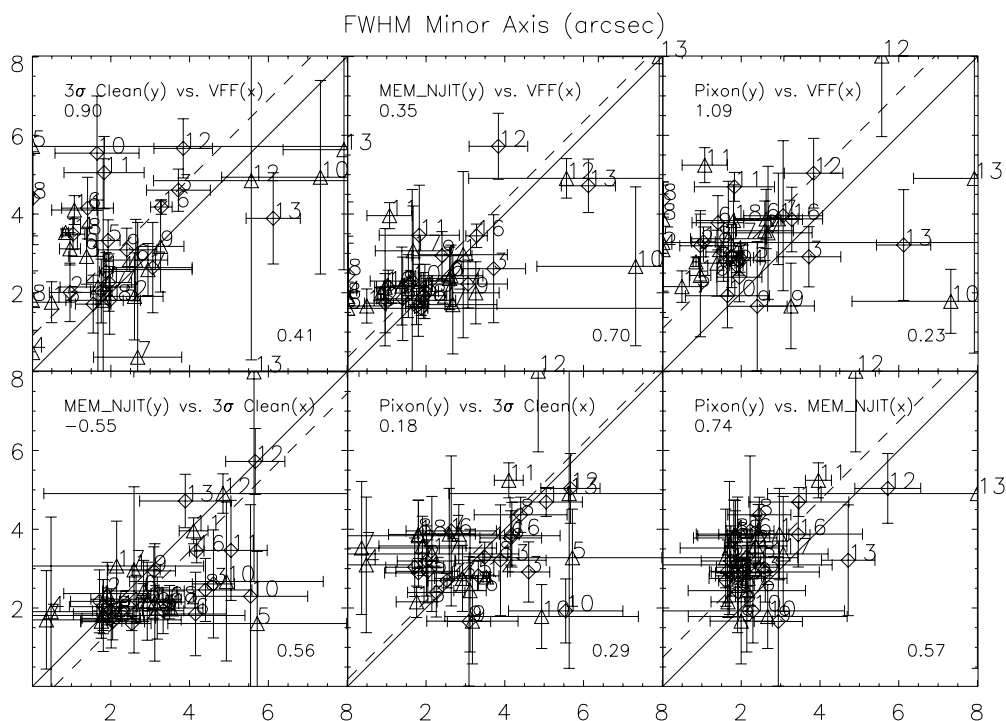
Figure 6. Minor axes comparison. Axis labels follow template used in Figure 4. The numbers in the upper left denote the average difference between minor axis measurements in the *y*-direction and minor axis measurements in the *x*-direction. The dashed line represents this systematic shift in the $y = x$ line.
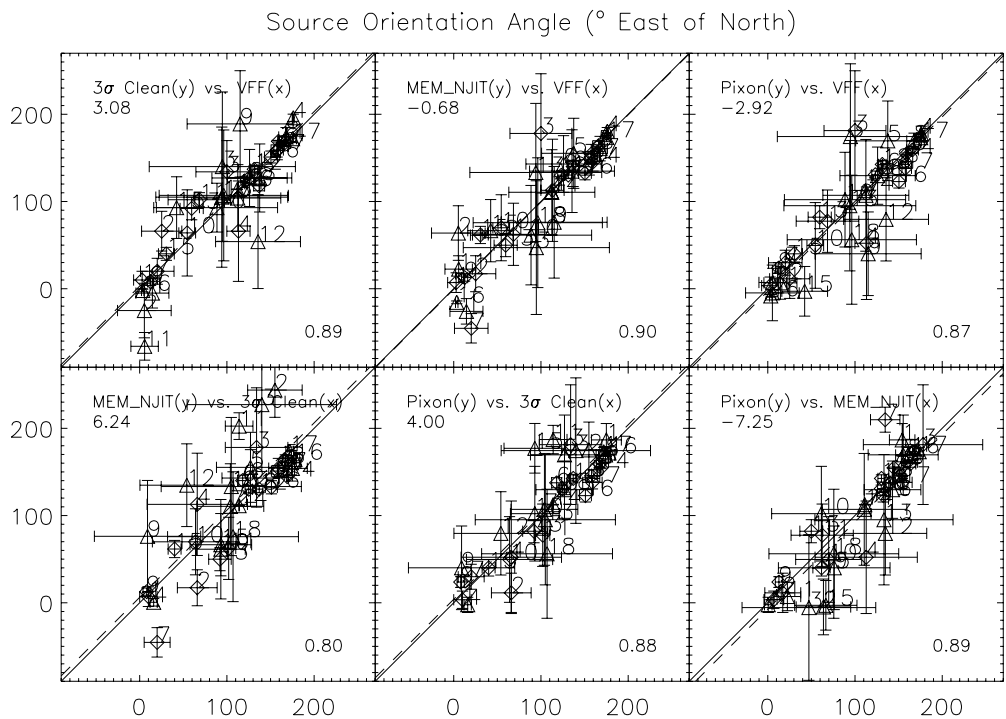

Figure 7. Plots of source orientation angle measurements for both footpoints of all 18 flares in our sample. Angles are measured counterclockwise from Solar north. Axis labels follow the template used in Figure 4. The numbers in the upper left of each plot are the average difference between the orientation angle in the *y*-direction and the orientation angle in the *x*-direction, and the dashed line represents this systematic shift of the $y = x$ line.

sources identified and fitted in the current study. Thus, they should give more reliable results than *VFF* in those cases where two elliptical Gaussians are inadequate to describe the source configuration in the image.

As evidence of additional flux in the reconstructed *Clean*, *MEM_NJIT*, and *Pixon* maps, we have compared the flux in the two identified sources with the total flux seen with *RHESSI* in

the same time interval and energy bin. For each algorithm, we have integrated the flux over the entire reconstructed image, thus calculating the total flux seen by *RHESSI* in this time interval and energy range. Then, the fluxes of the two sources identified by the user are summed. The ratio of the total source flux to the total flux of the map is plotted in the *Y*-direction of Figure 11. A ratio of unity implies a map whose flux contributions come
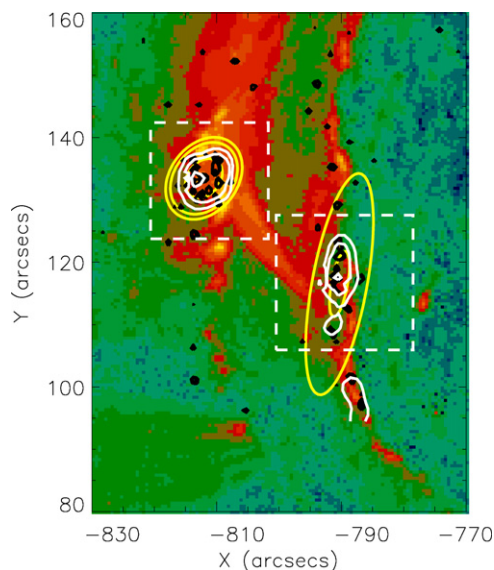
Figure 8. *RHESSI* contours overlaid on a *TRACE* 171 Å image (offset by +6″ and −16″ in heliocentric E–W and N–S directions, respectively, to match the near coincident EIT 195 Å image) for the flare on 2005 July 30. The 50–100 keV *RHESSI* images are for a time interval during the impulsive phase from 06:30:30 to 06:33:30 UT, while the *TRACE* image is for a short exposure near the center of that interval at 06:31:58 UT. The contours are at 5%, 10%, and 50% of the image maximum in each case with the following color code: black, *Clean* components; white, pixon; and yellow, *VFF*.

entirely from the two user-defined sources. In the *X*-direction, we have plotted the ratio of the total flux of the two sources calculated using *VFF* to the total flux of the two sources using the other algorithms. If this ratio approaches unity, then there is good agreement between the fluxes of the two sources in *VFF* and the other reconstruction algorithm.

From Figure 11, we see that the summed flux in the two sources in the *MEM_NJIT* and *Pixon* images is generally less than ∼80% of the total flux indicating additional flux contributions from other sources. Those additional flux contributions tend to be at a level of ≈1% of the maximum of the map but spread over a large number of pixels. The *Clean* images generally show a higher percentage of the flux in the two identified sources but this is presumably because we just considered the *Clean* components alone rather than adding in the total residual flux in the overall image. The summed flux of the two sources in the *VFF* images is always greater than the corresponding summed flux from the other algorithms with the difference becoming larger as the indication of additional flux in the image becomes greater, i.e., the ratios plotted in the *X*-direction in Figure 11 are all >1 and they tend to increase as the ratios plotted in the *Y*-direction decrease. We conclude that *VFF* is taking some of the small flux contributions from the whole map, or fluxes from a third source or additional sources, and adding them into the fluxes for the two assumed sources. This presumably accounts for the consistently higher fluxes obtained with *VFF* compared to the values obtained with the other three algorithms that is evident in Tables 2 and 3, and in Figure 4.

4. CONCLUSIONS

The objective of this study of *RHESSI* HXR flares is to obtain accurate and reliable measures of the dimensions of compact HXR sources seen with *RHESSI*. We chose 18 flares for analysis based on the presence of two compact HXR sources that were revealed in quicklook images above 25 keV. In carrying out the
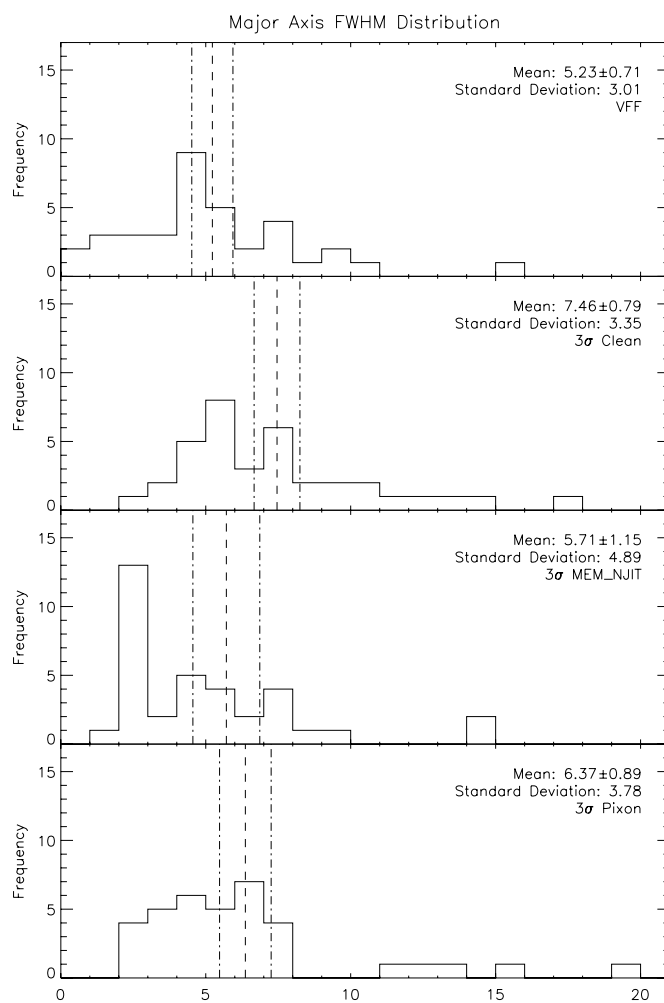

Figure 9. Source size distribution for the modified version of *VFF*, *Clean*, *MEM_NJIT*, and *Pixon*. Histogram bins represent the length in arcseconds of the major axes of every footpoint in our sample. Dashed lines represent the mean of each distribution and the dash-dotted lines show ±1σ on the mean.

study, we made use of all four of the currently available imaging algorithms—*Clean*, *Pixon*, *MEM_NJIT*, and *VFF*. Since *VFF* assumes Gaussian sources, we extended that assumption to the other algorithms so that comparable source parameters could be determined in each case. *VFF*, itself, was enhanced to allow for two elliptical Gaussians. We also used *Clean* in a nonstandard way by using the *Clean* point source components themselves to estimate source sizes. This eliminated the smearing effects of both the convolution with the *Clean* beam and the inclusion of the residuals in the default *Clean* images.

We found that source fluxes derived from all four algorithms are generally strongly correlated, as expected. The correlation coefficient for flux comparisons between the four methods are all ⩾0.97, but *VFF* systematically overestimates the flux compared to the other methods by a factor as large as two. The reason for this discrepancy is believed to be related to the inadequacy of the assumption that there were only two compact sources in each image (see below). Perhaps surprisingly, the *Clean* flux values were systematically higher than both the *Pixon* and *MEM_NJIT* values. This may be because *Clean* does not separate the compact and extended sources as well as *Pixon* and *MEM_NJIT* and consequently includes some of the flux from the extended sources in the flux of the compact sources.
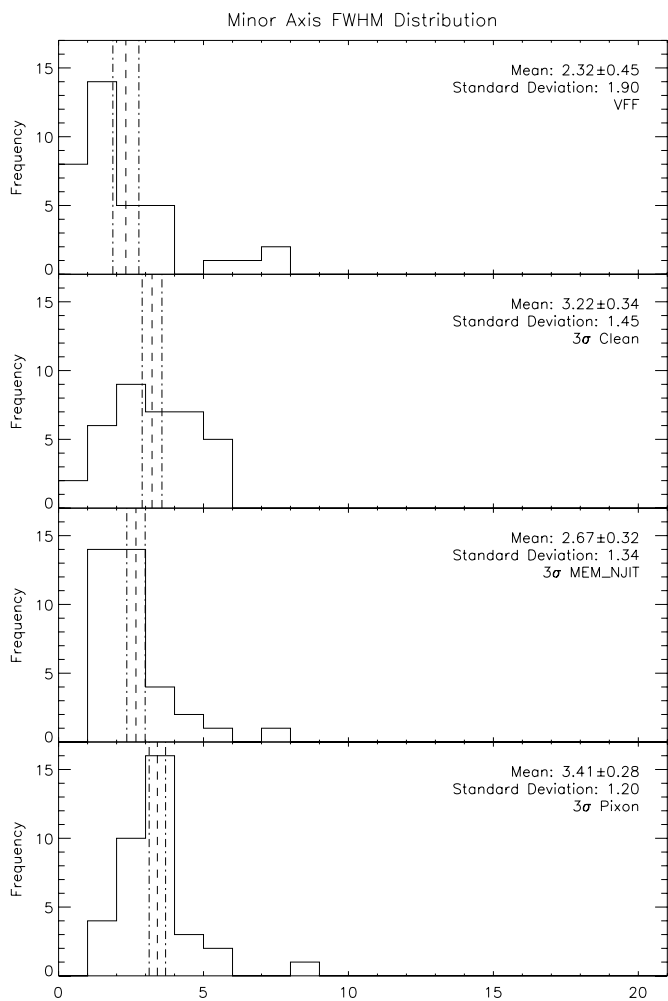
Figure 10. Same as Figure 9 for the minor axis FWHM distributions.

Figure 11. Plots to visualize the extent to which *VFF* fluxes overestimate the true source fluxes. The *Y*-axis is the ratio of the summed two-source fluxes to the total flux integrated over the whole image for the three algorithms except for *VFF*. A value of less than unity would indicate that some of the flux detected with RHESSI must come from other sources in addition to the two identified by the user. The *X*-axis is the ratio of the summed two-source fluxes obtained from *VFF* to the summed two-source fluxes obtained from the other three algorithms. A value differing from unity suggests that the two-source model assumed in *VFF* is not consistent with the observations.

The source sizes are also generally well correlated. The FWHM dimensions of the fitted elliptical Gaussian sources determined from the four algorithms are correlated with a coefficient of >0.6 for the major axis but as low as 0.25 for the minor axis. The correlation coefficients between *Pixon* and *MEM_NJIT* FWHM values are significantly better—0.94 for the major axis and 0.56 for the minor axis—presumably the result of their common use of maximum entropy. The correlations with parameters derived using *VFF* are significantly worse because of the much larger sizes obtained for a few events where the assumption that only two elliptical Gaussian sources are present in the image is incorrect.

The correlation coefficients for the source orientation angles are surprisingly high—⩾0.8 in all cases—suggesting that these angles provide a reliable indication of the alignment of the elliptical sources on the Sun. In the one case we were able to investigate that one of the two elliptical sources was positioned with its major axis aligned with a ribbon seen with *TRACE* at 171 Å. The other, almost circular source was positioned at a bright patch where the second ribbon made a right-angle turn. In another case not included in our list, Kontar et al. (2008) reported a limb flare with two HXR sources. We have verified that the orientation of these two sources is north–south as expected if the Kontar et al. (2008) interpretation that these two sources are footpoints seen at the limb so that the east–west dimension reflects the altitude extent of the source and the north–south dimension is the extent along the ribbons.
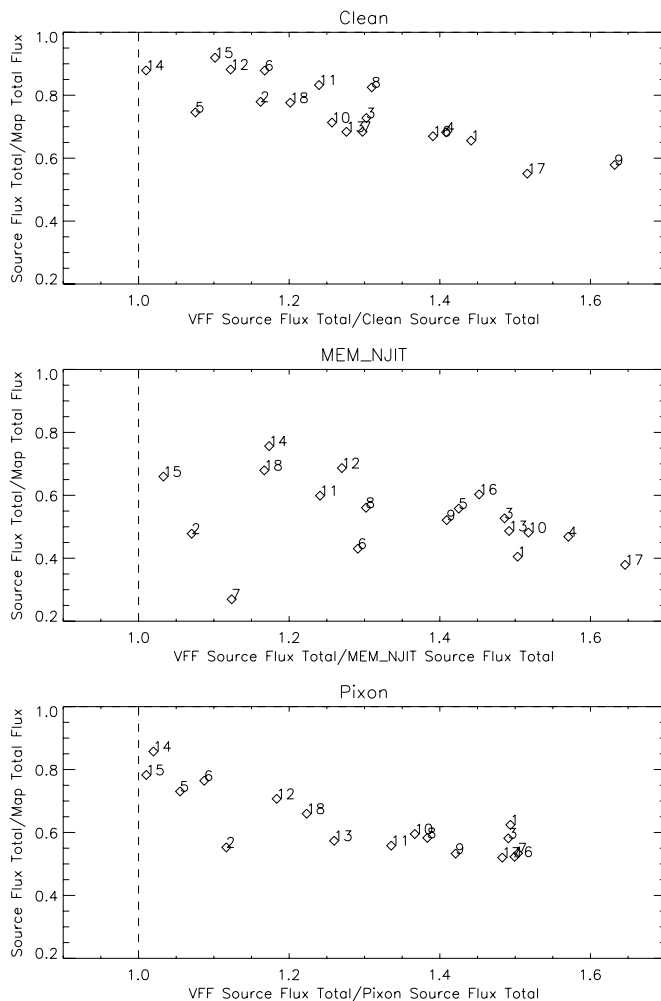
Given the good correlation between the ellipse major axis dimensions and orientation angles, and the alignment with solar features in the cases we have been able to check, it seems that these aspects of the sources are reliably measured. However, the relatively poor correlations found for the minor axis FWHM values suggests that the smallest dimension of the sources are not well measured. This may be the result of the limited "*uv*" coverage of the *RHESSI* observations making it difficult to determine unambiguous values for the 12 free parameters of the two assumed elliptical Gaussians. However, it is consistent with the sources being relatively thin ribbons similar in width to the Hα and EUV ribbons but covering only a small part of their length. Approximating such a shape with an elliptical Gaussian will inevitably give an overestimate of the width. Furthermore, the *RHESSI* collimators modulate the X-ray transmission to the detectors behind the finest grids only when the slits are closely aligned with the long axis of such thin ribbons. This again makes determining the width of such ribbonlike structures extremely difficult especially if they are curved. The maximum entropy method could compound this problem by effectively

smoothing out the modulation over the very narrow range of roll angles expected for thin ribbon sources. As a result of these considerations, it appears that measured minor axis values of $\lesssim 4''$ should be considered as upper limits.

The frequency distributions of the source sizes determined from the four different algorithms all show FWHM values ranging from the *RHESSI* resolution limit of $\sim 2''$ up to $\sim 20''$ with the same mean value within uncertainties of $7 \pm 1''$ for the major axis and $3 \pm 0''.4$ for the minor axis. The *MEM_NJIT* distribution shows more sources with dimensions below the mean value than do the other algorithms possibly reflecting its super-resolution ability (Cornwell & Evans 1985; Narayan & Nityananda 1986) although this cannot be verified here.

Evidence that the assumption of two elliptical Gaussians is inadequate to describe the source structure in many of these 18 flares is provided by comparing the summed fluxes in the two sources with the total flux in the whole image. In most events, less than 80% of the flux appeared in the two sources. *Clean* was somewhat better in this respect with more events above the 80% level than for *Pixon* or *MEM_NJIT*. This is possibly the result of an extended pedestal not removed from the *Clean* images for each source. *VFF*, on the other hand, suffered the most from this since it alone does not currently allow for any possibility of extended sources in addition to the two Gaussians. Consequently, the total fluxes in the two compact sources calculated with *VFF* were up to 100% higher than the fluxes calculated with the other three methods.

As the result of our study, we conclude that with careful use of the existing image reconstruction algorithms, reliable estimates can be made of the dimensions of compact HXR sources. Any one of the four algorithms can be used with the following provisos:

Clean

1. Can be safely used for compact sources to give similar results to the other algorithms.
2. Use the default settings with the following exceptions:
    a. Use the finest grids where possible to determine the level of fine-scale structure in the image. Then choose the grids and weighting to use based on the actual size of the source components. Note that detector 2 generally cannot be used below ~ 20 keV because of poor energy resolution and high threshold energy.
    b. Use uniform weighting only if there is sufficient modulation in the finest grids.
3. Use only the *Clean* point-source components themselves to determine the source sizes.
4. Do not use for extended sources, especially in the presence of compact sources.

Pixon

1. Can provide reliable estimates of source parameters.
2. Procedure is very slow taking over an hour to generate a single 128×128 pixel image even on a fast computer. Various techniques are available to speed it up so that a 64×64 pixel image can be generated in <15 minute on a fast PC with $\geqslant 4$ GB of memory.
3. Should only be used for final detailed analysis after the basic images have been made using *Clean*.
4. No new compact features are revealed by *Pixon* that are not also evident in fully optimized *Clean* images.
5. Tends to reject data for detectors 1 and 2 even if there is evidence for modulated count rates. The image can break

up into small sources unless the user-controlled parameter, pixon_sensitivity, is increased.
6. Currently, *Pixon* is the only way to adequately image extended sources in the presence of compact sources.

MEM_NJIT

1. Similar to *Pixon* but uses visibilities and is much faster.
2. Does not handle the finest grids well in some cases with source breaking up into small components.
3. Capable of super-resolution but this is not well understood or documented at this time.

VFF

1. Uses visibilities and is very fast, generally taking <1 minute per image.
2. Critical to verify that the required assumptions about the number of sources (maximum of two) and their shapes are adequate for the image being analyzed.
3. Currently, the only algorithm that provides uncertainties on the source parameters.
4. Overestimates source fluxes and dimensions when there are other sources in addition to those assumed to exist in the image.

Finally, it seems that the HXR source dimensions determined from *RHESSI* observations are accurate and reliable provided that there are adequate statistics and that the precautions discussed here are taken in using the different image reconstruction algorithms. The smallest dimension of many of the sources included in this paper are upper limits at about $4''$. This is consistent with the assumption that bright HXR sources are sections of flare ribbons seen at other wavelengths that are $\sim 1''$ wide but many arcseconds long. Any estimate of the source area for the determination of electron flux densities must allow for this possibility.

REFERENCES

Alexander, D., & Daou, A. G. 2007, ApJ, 666, 1268

Alexander, D., Metcalf, T., & Hudson, H. S. 1997, in ASP Conf. Ser. 111, Magnetic Reconnection in the Solar Atmosphere, ed. R. D. Bentley & J. T. Mariska (San Francisco, CA: ASP), 253

Allred, J. C., Hawley, S. L., Abbett, W. P., & Carlsson, M. 2005, ApJ, 630, 573

Aschwanden, M. J., Schmahl, E., & the *RHESSI* Team 2002, Sol. Phys., 210, 193

Brown, J. C. 1971, Sol. Phys., 18, 489

Cornwell, T. J., & Evans, K. F. 1985, A&A, 143, 77

Fisher, G. H., Canfield, R. C., & McClymont, A. N. 1985, ApJ, 289, 414

Fletcher, L., Hannah, I. G., Hudson, H. S., & Metcalf, T. R. 2007, ApJ, 656, 1187

Hannah, I. G., Christe, S., Krucker, S., Hurford, G. J., Hudson, H. S., & Lin, R. P. 2008, ApJ, 677, 704

Hoyng, P., et al. 1981, ApJ, 246, L155

Hurford, G. J., et al. 2002, Sol. Phys., 210, 61

Jess, D. B., Mathioudakis, M., Crockett, P. J., & Keenan, F. P. 2008, ApJ, 688, L119

Kontar, E. P., Hannah, I. G., & MacKinnon, A. L. 2008, A&A, 489, L57

Kosugi, T., et al. 1991, Sol. Phys., 136, 17

Krucker, S., et al. 2008, A&AR 8

Lin, R. P., et al. 2002, Sol. Phys., 210, 3

Liu, C., Lee, J., Gary, D. E., & Wang, H. 2007, ApJ, 658, L127

Metcalf, T. R., Hudson, H. S., Kosugi, T., Puetter, R. C., & Pina, R. K. 1996, ApJ, 466, 585

Milligan, R. O., Gallagher, P. T., Mathioudakis, M., Bloomfield, D. S., Keenan, F. P., & Schwartz, R. A. 2006a, ApJ, 638, L117

Milligan, R. O., Gallagher, P. T., Mathioudakis, M., & Keenan, F. P. 2006b, ApJ, 642, L169

Narayan, R., & Nityananda, R. 1986, ARA&A, 24, 127

Saint-Hilaire, P., von Praun, C., Stolte, E., Alonso, G., Benz, A. O., & Gross, T. 2002, Sol. Phys., 210, 143

Schmahl, E. J., Pernak, R. L., Hurford, G. J., Lee, J., & Bong, S. 2007, Sol. Phys., 240, 241

Shibata, K. 1998, in Astrophysics And Space Science Library 229, Observational Plasma Astrophysics: Five Years Of Yohkoh And Beyond, ed. T. Watanabe & T. Kosugi (Dordrecht: Kluwer), 187

Shibata, K., Masuda, S., Shimojo, M., Hara, H., Yokoyama, T., Tsuneta, S., Kosugi, T., & Ogawara, Y. 1995, ApJ, 451, L83

Tsuneta, S. 1997, ApJ, 483, 507

Tsuneta, S., et al. 1984, ApJ, 280, 887

Wang, H.-M. 2009, Res. Astron. Astrophys., 9, 127

Wang, L., Fang, C., & Ming-DeDing, 2007, Chin. J. Astron. Astrophys., 7, 721

Xu, Y., Emslie, A. G., & Hurford, G. J. 2008, ApJ, 673, 576